TÜBİTAK

Turkish Journal of Chemistry

http://journals.tubitak.gov.tr/chem/

Research Article

Turk J Chem
(2018) 42: 1251 – 1264

doi:10.3906/kim-1801-89

Synthesis, sintering, electrical properties, and sodium migration pathways of new lyonsite $Na_2Co_2(MoO_4)_3$

Rawia NASRI[1], **Riadh MARZOUKI**[2,*], **Samuel GEORGES**[3], **Saïd OBBADE**[3], **Mohamed Faouzi ZID**[1]

[1]Laboratory of Materials, Crystallochemistry and Applied Thermodynamics, Department of Chemistry, Faculty of Sciences, University of Tunis El Manar, El Manar II, Tunis, Tunisia

[2] Department of Chemistry, College of Science, King Khaled University, Abha, Saudi Arabia

[3]CNRS, LEPMI, F-38000 Grenoble, France

Received: 27.01.2018 • **Accepted/Published Online:** 28.05.2018 • **Final Version:** 11.10.2018

Abstract: A new double molybdate $Na_2Co_2(MoO_4)_3$ was synthesized via solid-state reaction and characterized by single-crystal X-ray diffraction (XRD). This compound is a new member of the lyonsite structure type. It crystallized in the orthorhombic system, space group Pnma with cell parameters $a = 5.272(2)$ Å, $b = 10.816(3)$ Å, and $c = 18.064(3)$ Å. The structure can be described as a three-dimensional framework with hexagonal tunnels in which the Na^+ cations lie. The obtained structural model is supported by charge distribution analysis and bond valence sum validation tools. Fourier-transform infrared spectroscopy and scanning electron microscopy analyses were carried out. Ball milling was used to reduce the particle size of the synthesized powder. Dense ceramics with a relative density of 78% were obtained by sintering at 853 K. The conductivity of the title compound was studied for different relative densities. The ionic conductivity at 723 K with an activation energy of 1.2 eV was 3.24×10^{-6} S cm^{-1}. The bond valence sum map model is used to simulate the cation migration pathways in the anionic framework.

Key words: Solid state reaction, lyonsite, sintering, electrical properties

1. Introduction

Over the past decades, inorganic materials with open frameworks have attracted much attention due their interesting properties and their potential applications in many fields, such as electric, magnetic, state laser materials, and the catalytic process.[1–6] In particular, a great number of materials in the Na–M–X–O (M = Co, Mn, Fe; X = Mo, P, V, As) systems have been investigated as positive electrode materials in new generation Na-ion batteries and might become competitive to Li-ion batteries.[7–14]

A rigorous examination of lyonsite family minerals found in the literature reveals previous studies of the family formulation $AM'(MoO_4)_3$, (A: cation; M′ = Mg, Cr, Co, Ti) treated many interesting properties, particularly ionic conductivity, in relation to their structures.[15–20] Moreover, it has been shown that in $Ag_4Co_7(AsO_4)_6$,[21] $Na_4Co_7(AsO_4)_6$,[22] $NaCo_2As_3O_{10}$,[23] and LAMOX ceramics[24,25] the electrical properties are closely related to the relative density, which points out the importance of its control. According to this approach, we decided to explore the Na_2O–CoO–MoO_3 ternary system. Furthermore, these structural characteristics encouraged us to study the electrical properties. In this paper, we present the synthesis, crystal

*Correspondence: riadh.marzouki@hotmail.fr

structure, and infrared spectroscopy of $Na_2Co_2(MoO_4)_3$. Particular attention was paid to the importance of density control of ceramics, which dramatically affects the measured electrical properties, particularly conductivity. A theoretical study is carried out to identify the probably sodium pathways in the anionic framework.

2. Results and discussion

2.1. Structure refinement and validation

A suitable blue single crystal with dimensions 0.11 × 0.11 × 0.17 mm^3 was selected under a polarizing microscope. The crystal data were collected on an Enraf–Nonius CAD-4 diffractometer (Rotterdam, the Netherlands) using Mo Kα (λ = 0.71073 Å) radiation at room temperature.[26,27] The refinement was solved against F^2 in the crystal structure. All calculations were performed using the SHELX-97 computer programs incorporated in the WinGX software package.[28,29] The structure has been solved in the centrosymmetric space group Pnma. Two molybdenum and cobalt atoms were first located. Then three oxygen atoms, sodium, and cobalt were found by successive Fourier difference synthesis. At this stage, the agreement reliability factor was 0.058. Then the use of the SUMP instruction of SHELX-97 decreased the reliability factors to R = 0.032 and wR = 0.70. All atoms were anisotropically refined. Absorption correction via a psi-scan was applied to correct for polarization and Lorentz effects.[30] The agreement factors R and wR converged to 0.026 and 0.067, respectively. The proposed structural model was confirmed by the two structural tools, bond valence sum (BVS) and charge distribution analysis (CHARDIT).[31–34] BVS and CHARDIT show adequate valences (V) and charges (Q) of all the cation sites. The structural model was thus validated and the dispersion factor was 2.2%, which measures the deviation of the calculated Q with respect to the formal oxidation numbers. The bond valence computation and charge distribution analysis are summarized in Table 1. The details of the structure refinement, final agreement factors, and crystallographic data are given in Table 2. The atomic coordinates and isotropic displacement parameters are listed in Table 3. The main interatomic distances are given in Table 4.

Table 1. CHARDIT and BVS analysis of cation polyhedral in $Na_2Co_2(MoO_4)_3$.

Cation	$q(i)$.sof(i)	$Q(i)$	$V(i)$	CN(i)	ECoN(i)
Mo1	6	6.09	5.87	4	3.99
Mo2	6	5.95	5.81	4	3.97
M1	1.67	1.65	1.83	6	5.88
M2	1.67	1.69	1.68	6	5.85
Na3	1	0.99	1.02	6	5.95

M(1) = Na(1)/Co(1), M(2) = Na(2)/Co(2), $q(i)$ = formal oxidation number, sof(i) = site occupation factor, $Q(i)$ = calculated charge, CN(i) = coordination number, ECoN = effective coordination number, $\sigma_{cat} = [\Sigma i(q_i - Q_i)^2 / N - 1]^{1/2} = 0.022$.

Rietveld refinement was performed in the 6–70° range using the single crystal structure operating JANA2006 software.[35,36] The final agreement factors are Rp = 0.02, Rwp = 0.033, and $R(F^2)$ = 0.067 (Figure 1).

2.2. Crystal structure

The title compound is a new member of the lyonsite family. It crystallizes in the Pnma space group of the orthorhombic system. The structural unit in the compound is formed by two octahedra MO_6 (M = Co/Na)

Table 2. Crystal data and refinement parameters for $Na_2Co_2(MoO_4)_3$.

Formula	$Na_2Co_2(MoO_4)_3$
Formula weight	643.66
Crystal size	$0.11 \times 0.11 \times 0.17$ mm^3
Color	Blue
Crystal system	Orthorhombic
Space group	Pnma
Unit cell dimensions	a = 5.272(2) Å; b= 10.816(3) Å; c = 18.064(3) Å
Volume; Z	1030.10(5) Å^3; 4
Absorption coefficient	6.85 mm^{-1}
Scan mode	$\omega/2\theta$
θ max	27°
Index range	$-6 \leq$ h ≤ 5; $-1 \leq$ k ≤ 13; $-1 \leq$ l ≤ 23
Measured reflections	2358
Independent reflections	1172
Reflections $I > 2\ \sigma I$	916
Refinement method	Full matrix least squares on F^2
Data/parameters	916/95
Final R	$R = 0.026 :\ wR = 0.067$
Largest diff. peak and hole (e.Å^{-3})	0.93 and −1.03

Table 3. Fractional atomic coordinates and isotropic displacement parameters (Å^2) in $Na_2Co_2(MoO_4)_3$.

Atom	Wyckoff position	x	y	z	U^*_{eq} (Å)	Occ (<1)
Mo1	4c	0.22144 (1)	0.2500	0.44340 (3)	0.01237 (2)	
Mo2	8d	0.72251 (9)	0.51825 (4)	0.34517 (2)	0.01132 (2)	
Co1	4c	0.4010 (3)	0.2500	0.25069 (8)	0.0248 (4)	0.338 (2)
Na1	4c	0.4010 (3)	0.2500	0.25069 (8)	0.0248 (4)	0.161 (2)
Co2	8d	0.75364 (2)	0.42776 (9)	0.52646 (5)	0.0109 (2)	0.668 (5)
Na2	8d	0.75364 (2)	0.42776 (9)	0.52646 (5)	0.0109 (2)	0.331 (6)
Na3	8d	0.2458 (5)	0.7500	0.30504 (2)	0.0147 (6)	
O1	8d	0.9034 (8)	0.6138 (4)	0.2895 (2)	0.0227 (9)	
O2	4c	0.9519 (1)	0.2500	0.5043 (3)	0.0252 (1)	
O3	8d	0.4497 (8)	0.6011 (4)	0.3756 (2)	0.0241 (1)	
O4	8d	0.9158 (8)	0.4843 (4)	0.4248 (2)	0.0171 (8)	
O5	4c	0.1450 (1)	0.2500	0.3476 (3)	0.0186 (1)	
O6	8d	0.6488 (7)	0.3792 (4)	0.2961 (2)	0.0182 (8)	
O7	8d	0.4122 (8)	0.1196 (4)	0.4635 (2)	0.0194 (9)	

*U_{eq} is defined as one-third of the trace of the orthogonalized U_{ij}

Table 4. Main interatomic distances (Å) in the coordination polyhedra.

Mo1 tetrahedron		M1 octahedron	
Mo1—O7^{i}	1.770 (4)	M1—O6	2.081 (4)
Mo1—O7	1.770 (4)	M1—O6^{i}	2.081 (4)
Mo1—O5^{ii}	1.777 (5)	M1—O6^{viii}	2.106 (4)
Mo1—O2^{ii}	1.797 (6)	M1—O6^{ix}	2.106 (4)
Mo2 tetrahedron		M1—O5^{ix}	2.192 (5)
Mo2—O1	1.728 (4)	M1—O5^{ii}	2.210 (6)
Mo2—O3	1.782 (4)	M2 octahedron	
Mo2—O6	1.789 (4)	M2—O3^{iv}	2.093 (4)
Mo2—O4	1.800 (4)	M2—O4	2.116 (4)
		M2—O4^{vii}	2.172 (4)
		M2—O7^{i}	2.190 (4)
		M2—O2	2.225 (3)
		M2—O7^{x}	2.259 (4)
		Na3 octahedron	
		Na3—O3	2.317 (4)
		Na3—O3^{xi}	2.317 (5)
		Na3—O1^{ii}	2.347 (5)
		Na3—O1^{xii}	2.347 (5)
		Na3—O1^{ix}	2.404 (4)
		Na3—O1^{xiii}	2.404 (4)

Symmetry codes: (i) x, $-y+$ 1/2, z; (ii) $x-$ 1, y, z; (iii) $x-$ 1, $-y+$ 1/2, z; (iv) $-x+$ 1, $-y+$ 1, $-z+$ 1; (v) $-x+$ 1, $y-$ 1/2, $-z+$ 1; (vi) $x+$ 1/2, y, $-z+$ 1/2; (vii) $-x+$ 2, $-y+$ 1,$-z+$ 1; (viii) $x-$ 1/2, $-y+$ 1/2, $-z+$ 1/2; (ix) $x-$ 1/2, y, $-z+$ 1/2; (x) $-x+$ 1, $y+$ 1/2, $-z+$ 1; (xi) x, $-y+$ 3/2, z; (xii) $x-$ 1, $-y+$ 3/2, z; (xiii) $x-$ 1/2, $-y+$ 3/2, $-z+$ 1/2.

attached by two tetrahedra MoO_4 arranged in a cyclic way. The charge compensation is provided by Na^+ cations (Figure 2). In the structure, each $M(1)O_6$ (M(1) = Co(1)/Na(1)) octahedron shares faces to form chains type M_1O_3. On the other hand, two octahedra $M(2)O_6$ (M(2) = Co(2)/Na(2)), juxtaposed, are connected via edges to form M_2O_{10} dimers. These dimers are connected by vertices, which lead to zigzag chains. The junction between these different chains is assured by MoO_4 tetrahedra sharing corners to form layers arranged parallel to the plane (010) (Figure 3). It results in a three-dimensional framework with hexagonal tunnels along the (100) direction in which the monovalent cations lie (Figure 4). The M cationic sites in the title compound are occupied by a mixture of Na1/Co1 and Na2/Co2 cations in ratios of 0.2:0.3 and 0.3:0.7, respectively. In the anionic framework, all molybdenum cations are in the tetrahedral environment MoO_4, with effective coordination numbers ECoN(Mo1) = 3.99 and ECoN(Mo2) = 3.97. The Mo—O distances are in the range 1.729(1) to 1.801(2) Å. The M—O bond lengths in the octahedra range from 2.081(2) to 2.259(1) Å, with effective coordination numbers ECoN(M1) = 5.88 and ECoN(M2) = 5.85. The Na—O interatomic distances in the polyhedron vary overall from 2.317(2) to 2.404(1) Å.

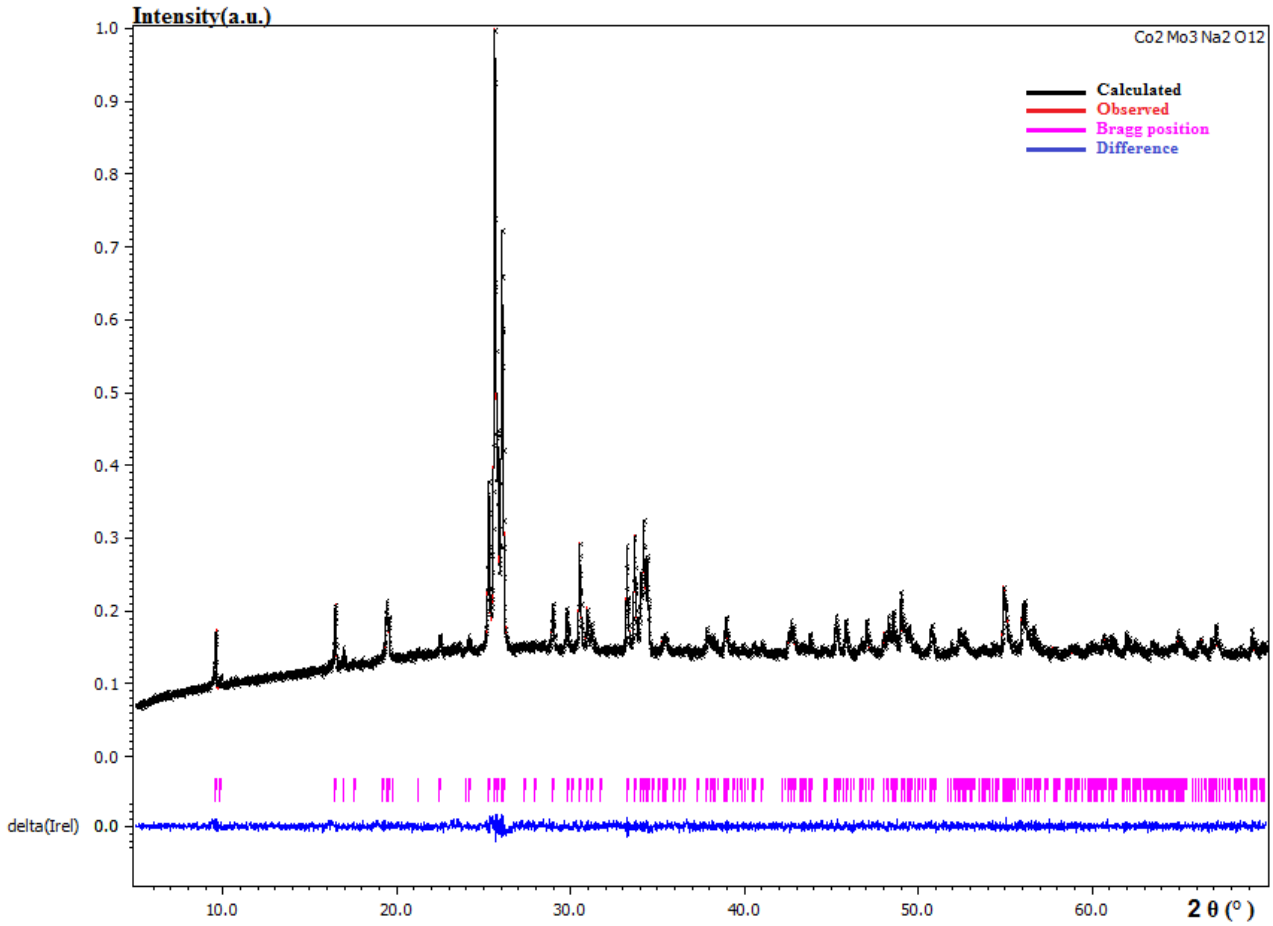

Figure 1. Rietveld refinement patterns of the sample.

2.3. Infrared (IR) spectroscopy

The IR spectrum of the title compound was recorded at room temperature in the range of 4000–400 cm^{-1}. We are interested only in the domain 1000–400 cm^{-1}, where principal IR vibrations are present (Figure 5). The bond observed at 935 cm^{-1} is attributed to ν_1 symmetric stretching vibration in MoO_4^{2-} tetrahedra. However, the absorption bonds at 851, 811, 775, and 721 cm^{-1} are assigned to the ν_3 vibrational modes related to Mo–O stretching vibration in the ionic MoO_4^{2-}. The bond located at 428 cm^{-1} is assigned to ν_4 bending mode vibrations. The assignment of different vibrational bands of MoO_4 tetrahedron, based on the literature, is shown in Table 5.[37–39]

Table 5. Assignment of vibration frequencies in $Na_2Co_2(MoO_4)_3$ compound.

Wave number (cm^{-1})	Assignment
935	ν_1 (MoO_4)
851, 811 775, 721	ν_3(MoO_4)
428	ν_4 (MoO_4)

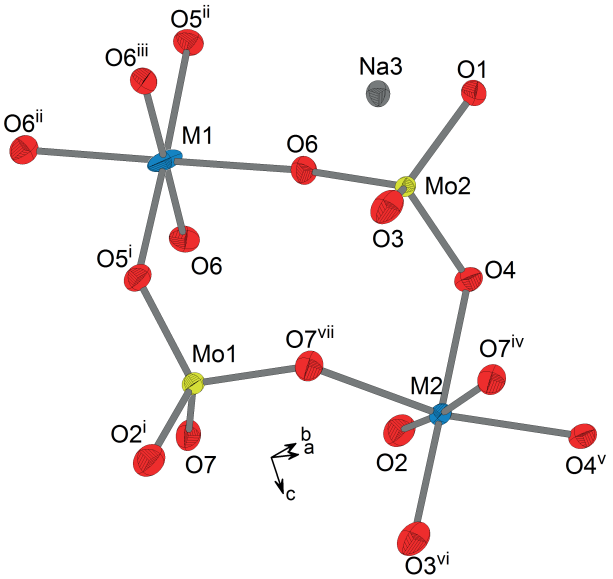

Figure 2. The coordination polyhedral in the structural unit of $Na_2Co_2(MoO_4)_3$. Displacement ellipsoids are drawn at the 50% probability level [symmetry codes: (i) –1 +x, y, z; (ii) –1/2 + x, 1/2 –y, 1/2 –z; (iii) –1/2 +x, y, 1/2 –z; (iv) 1 – x, 1/2 +y, 1 – z; (v) 2 –x, 1 – y, 1 –z; (vi) 1 –x, 1 – y, 1 –z; (vii) x, 1/2 – y, z.

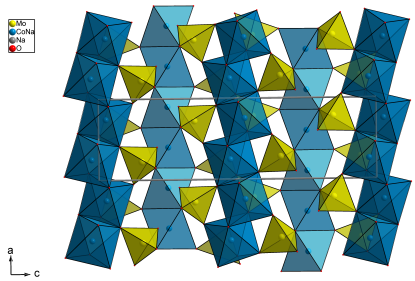

Figure 3. Projection of the layer along the [010] direction.

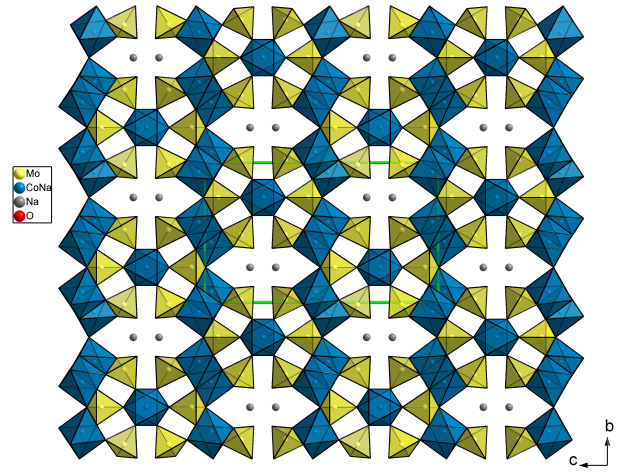

Figure 4. Projection of $Na_2Co_2(MoO_4)_3$ along the a axis.

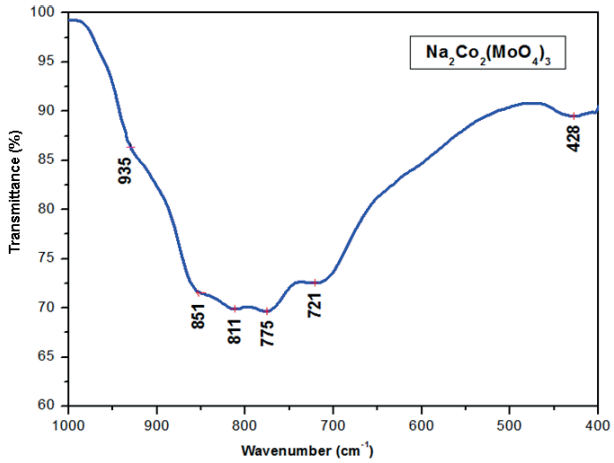

Figure 5. IR spectrum of the compound.

2.4. Control of the ceramics microstructure

In order to obtain accurate electrical properties, in particular to lower the contribution of microstructure, the densification of the raw powders was realized. First, the optimal sintering temperature was determined for pellets obtained from the initial unmilled powders. Increasing sintering temperatures were applied from 793 to 873 K for 2 h. The variation in the relative density of the $Na_2Co_2(MoO_4)_3$ ceramics via sintering temperature is shown in Table 6. The relative density increased from 57% to 66%. The optimal sintering temperature was then retained as 853 K. However, the relative density had to be further increased to lower the contribution

of porosity. In the second step, planetary ball milling was applied in order to reduce the particle size of the raw powder. Alternating 15 min milling sequences with 5 min pauses were applied for a total duration of 120 min. The gradual reduction of the mean particle size of the powder was confirmed by scanning electron microscopy (SEM) micrographs (Figures 6a–6c). In fact, the grains of the initial powder were not homogeneous. Some particles presented a size greater than 10 μm. After 120 min milling time, the sample showed better homogeneity. The average particle size was about 3 μm (Figure 6c).

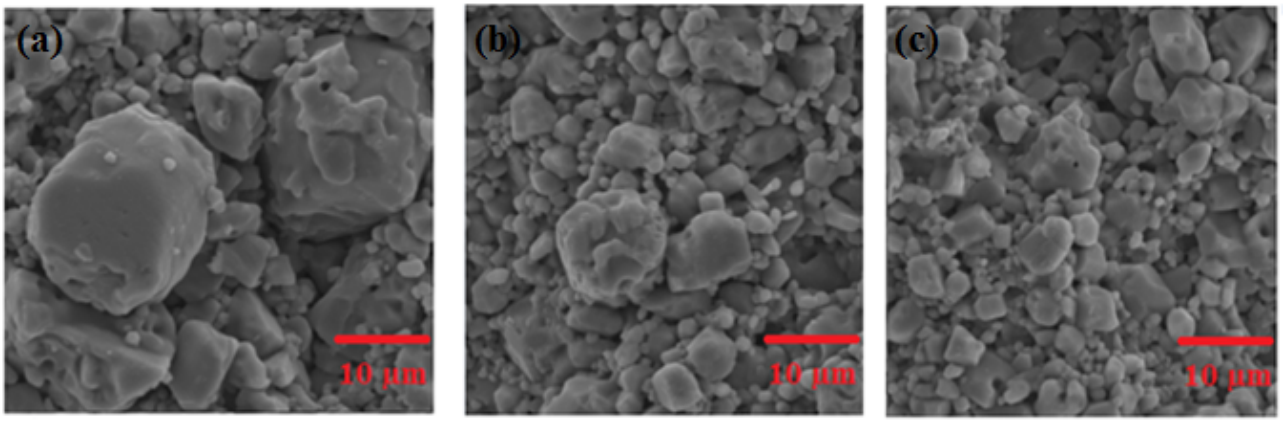

Figure 6. EM micrographs of $Na_2Co_2(MoO_4)_3$ powder after different milling time (a) 0 min, (b) 60 min, (c) 120 min.

Table 6. Variation of the relative densities of the $Na_2Co_2(MoO_4)_3$ initial powder upon sintering temperature.

Sintering temperature (K)	Relative density (%)
793	57
813	59
833	63
853	66
873	65

The reduction of $Na_2Co_2(MoO_4)_3$ powder particle size yielded a significant increase of the relative density from 66% (not milled) to 78% after 120 min of ball milling treatment. A relative density of 78% can be achieved for only 105 min total duration, 7 sequences of milling. There is no more variation of density after one additional sequence of 15 min of grinding. For this reason, we stopped milling after 7 sequences to limit the risk of contamination.[24]

2.5. Electrical properties

Electrical conductivity was investigated over a temperature interval from 453 K to 783 K using complex impedance spectroscopy over the range of 13 MHz–5 Hz.

The Nyquist plots recorded in air at 723 K for the sample with different relative densities (66%, 71%, and 78%) are shown in Figure 7a. The shift of the relaxation frequencies is shown in Figure 7b in the Bode plane. The Nyquist plot shows a single semicircular arc with capacities around $10^{-12}F$ cm^{-1} (Table 7). It shows that the electrical processes in the compound arise basically due to the contribution from the bulk material.[40,41] The

measured impedance can be modeled using an equivalent electrical circuit composed of a parallel combination of a resistor (R) and a constant phase element (CPE). The CPE is an empirical impedance function of the type:

$$Z(\omega)_{CPE} = 1/C(j\omega)^p; (-1 \leq p \leq 1),$$

where C is the true capacitance, ω is the frequency, and p is a parameter $(-1 \leq p \leq 1)$.

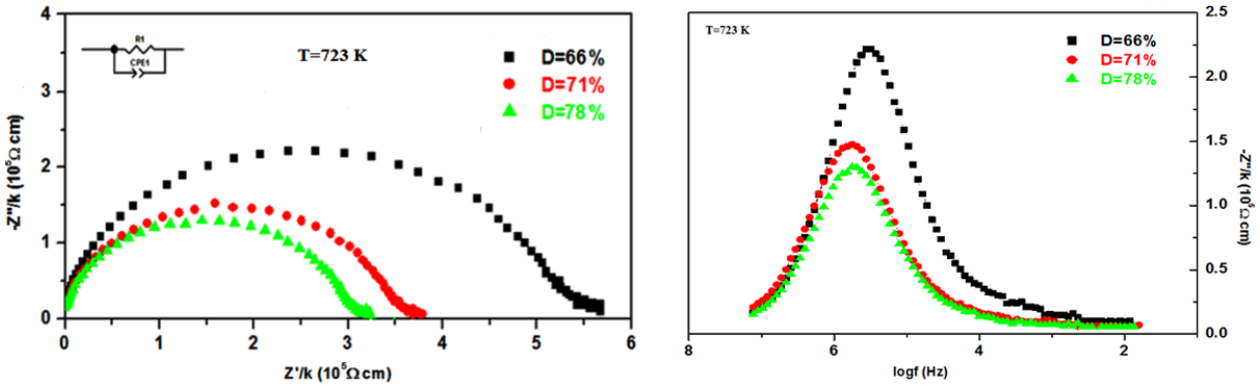

Figure 7. Impedance spectra recorded at 723 K in air on $Na_2Co_2(MoO_4)_3$ sample with different relative densities in air; (a) Nyquist plane; (b) Bode plane.

Table 7. Values of equivalent circuit electrical parameters calculated for impedance spectra measured at 723 K for different relative densities.

Density (%)	R (kΩ)	C (10^{-12} F)	k (cm^{-1})	C/k (10^{-12} F cm^{-1})	P	ρ (10^4 Ω cm)	σ (10^{-6} S cm^{-1})
66	198.04	2.48	0.37	6.70	0.87	53.52	1.87
71	135.93	1.94	0.38	5.11	0.87	35.77	2.80
78	123.81	2.34	0.40	5.85	0.87	30.87	3.24

Theoretical density = 4.15 g cm^{-3}.

Impedance analysis software Zview was used to simulate the impedance spectra.[42] The resistances, capacitances, and exponent values were easily calculated from the resulting fit. The refined electrical parameters of $Na_2Co_2(MoO_4)_3$ (with different densities) obtained from the equivalent circuit at 723 K are shown in Table 7.

A second contribution at low frequencies appears in the impedance spectra. Given its low magnitude compared to the high-frequency semicircles, this contribution was not taken into account when determining electrical conductivity. The influence of the relative density in $Na_2Co_2(MoO_4)_3$ oxide can be clearly observed in Figure 8. For example, the conductivity values for the double molybdate at 723 K increases from 1.87 × 10^{-6} S cm^{-1} and 2.80 × 10^{-6} S cm^{-1} to 3.24 × 10^{-6} S cm^{-1} for D = 66%, D = 71%, and D = 78%, respectively. In fact, resistivity is strongly related to ceramic porosity. Thus, a porosity of 12% lowers the conductivity to about 43% of that of the bulk material (D = 78%). This phenomenon was observed in the entire temperature range. The measured conductivity increased strongly from 66% to 71% of relative density, and slightly from 71% to 78%. This observation is presented in Figure 7. Then, from Figures 7 and 8, we can point out that the obtained conductivities for 78% of relative density are close to the specific values of the molybdate and that the influence of the microstructure has been lowered by the densification process.

Conductivity data can be fitted to straight lines in the Arrhenius representation and analyzed by an Arrhenius equation: $\sigma T = \sigma_0 \exp(-Ea/kT)$, where σ is the electrical conductivity, σ_0 is the preexponential

factor, k is the Boltzmann constant and T is temperature. We see that the evolution of $\ln(\sigma T)$ according to $1000/T$ is linear, with activation energies of 1.30 eV, 1.25 eV, and 1.20 eV for 66%, 71%, and 78% relative densities, respectively (Figure 9). This increase in the observed activation energy, previously observed in other materials,[21,22] describes the influence of porosity on electrical transport. In this case, optimal sintering conditions with control of the microstructure are a prerequisite for the electrical measurement.

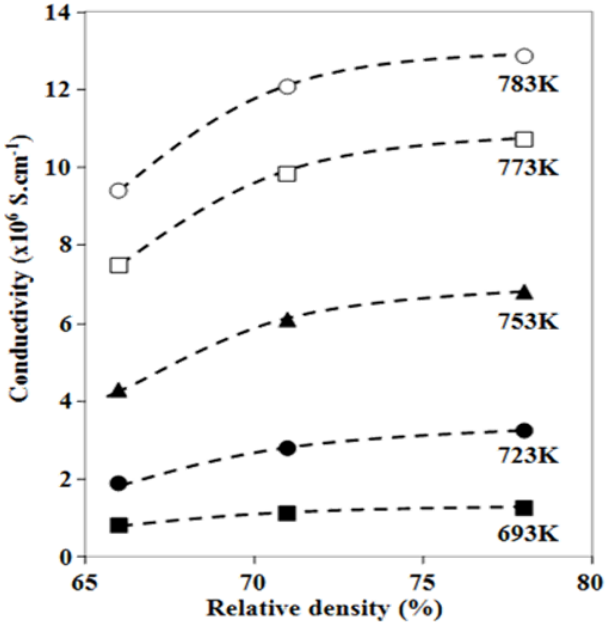

Figure 8. Conductivity as a function of relative density of $Na_2Co_2(MoO_4)_3$ ceramics at different temperatures.

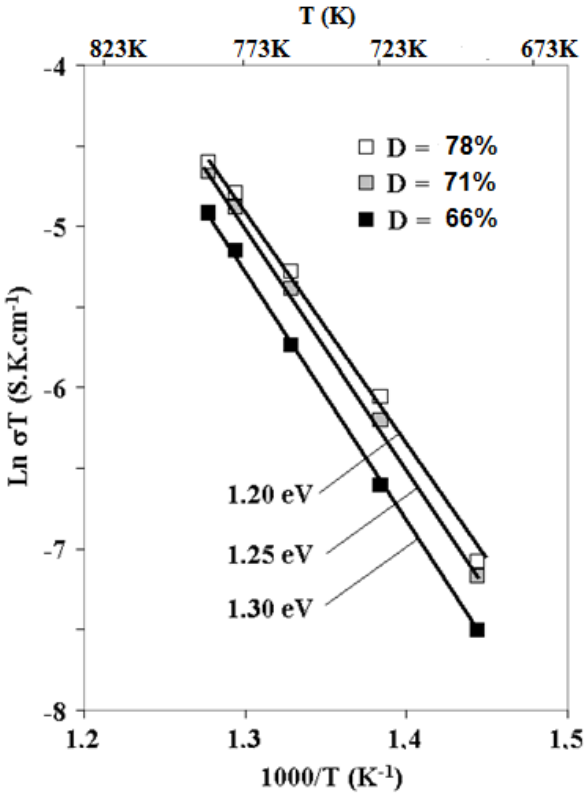

Figure 9. Arrhenius plots of conductivity of $Na_2Co_2(MoO_4)_3$ samples with various relative densities.

Comparing to other lyonsite families, such as $Li_2Mg_2(MoO_4)_3$ ($\sigma_{573\,K} = 1.1 \times 10^{-7}$ S cm^{-1}, Ea = 0.71 eV), $Li_{1.8}Mg_{2.1}(MoO_4)_3$ ($\sigma_{573\,K} = 6.1 \times 10^{-8}$ S cm^{-1}, Ea = 0.63 eV), $Li_{1.6}Mg_{2.2}(MoO_4)_3$ ($\sigma_{573\,K} = 1.4 \times 10^{-8}$ S cm^{-1}, Ea = 0.76 eV), $Li_{1.4}Mg_{2.3}(MoO_4)_3$ ($\sigma_{573\,K} = 1.0 \times 10^{-8}$ S cm^{-1}, Ea = 0.62 eV), $Li_3Fe(MoO_4)_3$ ($\sigma_{573\,K} = 6.6 \times 10^{-7}$ S cm^{-1}, Ea = 1.11 eV),[20] $Li_3Cr(MoO_4)_3$ ($\sigma_{873\,K} = 3.9 \times 10^{-3}$ S cm^{-1}, Ea = 1.06 eV),[16] and other molybdates, such as $LiMg_3VMo_2O_{12}$ ($\sigma_{773\,K} = 1 \times 10^{-3}$ S cm^{-1}, Ea = 0.8 eV),[43] $Na_5Sc(MoO_4)_4$ ($\sigma_{573\,K} = 6.44 \times 10^{-6}$ S cm^{-1}, Ea = 0.72 eV), $Na_{2.2}Zn_{0.9}(MoO_4)_2$ ($\sigma_{573\,K} = 7 \times 10^{-7}$ S cm^{-1}, Ea = 0.85 eV),[44] and $Na_2In_2Mo_5O_{16}$ ($\sigma_{548\,K} = 2 \times 10^{-7}$ S cm^{-1}, Ea = 0.79 eV),[45] the conductivity at 723 K 3.24×10^{-6} S cm^{-1} and the activation energy (Ea = 1.20 eV) show that $Na_2Co_2(MoO_4)_3$ is a medium ionic conductor.

2.6. Na^+ transport pathways simulation

The transport pathways of Na^+ ions in $Na_2Co_2(MoO_4)_3$ were simulated using the bond valence sum map model. This model was used with success to determine the pathways migration of Li^+ in Li_4GeS_4[46] and

Na^+ in $NaCo_2As_3O_{10}$.[23] The bond valence sum calculation was obtained using 3DBVSMAPPER computer program[47] in the bond valence energy landscape mode, as recently reported for $Na_4Co_7(AsO_4)_6$.[22] The results are depicted in Figure 10. This figure shows one-dimensional migration pathways for sodium along the a-axis with zigzag form and the isosurface with a bond valence activation energy of approximately 2.2 eV. Sodium transport pathways in $Na_2Co_2(MoO_4)_3$ were simulated based on single-crystal X-ray diffraction (XRD) data. The crystal structure showed hexagonal tunnels along the a-axis in which Na^+ cations lie (Figure 11). The tunnel was large, with a maximum cross of 9.260(1) Å measured between O atoms. Sodium atoms showed a high thermal agitation, which would be a factor for ionic conduction.

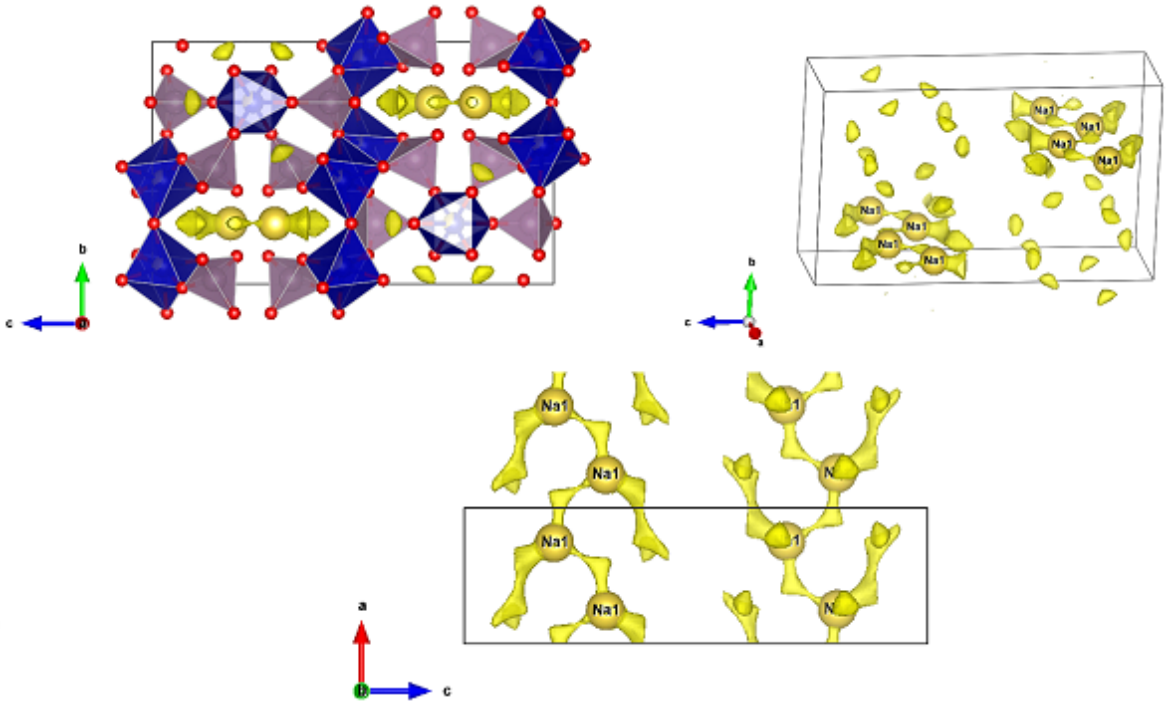

Figure 10. Bond valence site energy depicted as landscapes (isovalue 2.06 eV above the E_{min}) for Na^+ mobility in $Na_2Co_2(MoO_4)_3$.

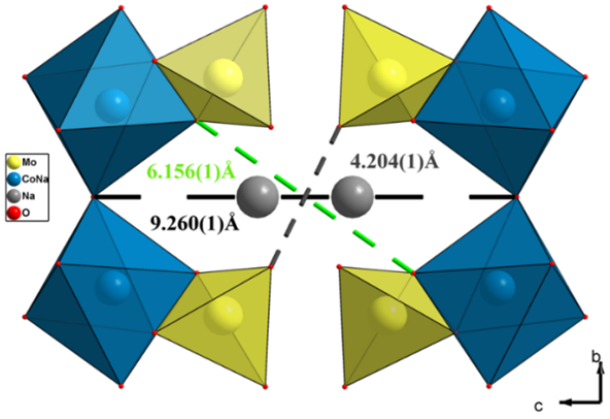

Figure 11. Dimensions of the tunnel along [100] direction.

2.7. Conclusions

Single crystals of the new compound, a member of the lyonsite family, were synthesized using a solid-state reaction. This material was characterized by single-crystal XRD. The sample crystallized in orthorhombic symmetry with Pnma space group ($Z = 4$) and the unit cell parameters are $a = 5.272(2)$ Å, $b = 10.816(3)$ Å, and $c = 18.064(3)$ Å. The structure of the title compound has an open three-dimensional framework with hexagonal tunnels along [100] direction in which the Na^+ cations lie.

Electrical measurements carried out by impedance spectroscopy complex show that the electrical properties appear to be strongly related to the relative density. In fact, the increasing mean density in the title material increased the ionic conductivity and decreased the apparent activation energy for the considered compound. The dense ceramics ($D = 78\%$) of the studied material present a conductivity of 3.24×10^{-6} S cm^{-1} at 723 K and an activation energy of 1.20 eV. This value of conductivity for $Na_2Co_2(MoO_4)_3$ is intermediate in the lyonsite family. This material can be tested as a cathode in Na-ion batteries.

3. Experimental

3.1. Equipment and materials

Qualitative analysis by SEM probe was performed using a FEI QUANTA 200 electron microscope (Hillsboro, OR, USA).

The IR spectrum was measured for a finely ground 2 mg sample with 160 mg of KBr, and then compressed under 1 kbar. The pellet was analyzed using an infrared spectrometer (PerkinElmer, Waltham, MA, USA) with Fourier transform over the range 4000 to 400 cm^{-1}, which contains the characteristic absorption bands of the studied phase.

A D8 Bruker diffractometer (Billerica, MA, USA) operating with copper anticathode Cu Kα ($\lambda = 1.5406$ Å) over the range of $10^\circ \leq 2\theta \leq 70^\circ$ was used to record XRD pattern at room temperature.

The electrical measurements were preceded by a pretreatment of the samples in order to reduce the mean particle size of the synthesized powders. Each sample was milled by a Fritsch planetary micromill pulverisette machine (Pittsboro, NC, USA) equipped with agate balls and agate jars. Each agate jar contained 5 g of powder and six agate balls. To avoid excessive heating and reduce pollution, the milling was carried out in ethanol. Pellet-shaped samples with different relative densities were obtained by uniaxial shaping, isostatic pressure at 2.5 kbar followed by a sintering in air at 773 K for 2 h in air with 5 K min^{-1} heating and cooling rates. Electrical measurements were made in air by complex impedance spectroscopy using a Hewlett Packard 4192 A frequency response analyzer (FRA) in the 13×10^6 Hz–5 Hz frequency range (Palo Alto, CA, USA). Fully covering 0.1 μm thick platinum layers were placed like electrodes on both faces of pellet by RF magnetron sputtering. Considering the low temperatures applied for the electrical analysis (723 K), this thickness was sufficient to avoid subsequent modification and platinum coalescence of the electrically active surface. The measurements were carried out at the open circuit voltage, with an applied AC voltage of 50 mV. The ceramics were connected to the FRA using platinum wires and grids. These latter were mounted in a stainless steel sample holder located inside an alumina tube and situated in a Pyrox furnace.

3.2. Synthesis of $Na_2Co_2(MoO_4)_3$

$Na_2Co_2(MoO_4)_3$ crystals were synthesized via solid-state reaction. The mixture of Na_2NO_3 (>99%, Fluka, Morristown, NJ, USA), $Co(NO_3)_2.6H_2O$ (99%, Fluka), and $(NH_4)_6Mo_7O_{24}$(>99%, Fluka), with an Na:Co:Mo

molar ratio of 2:2:3, was ground in an agate mortar and placed in a silica crucible. It was first heated at 623 K for 24 h. Thereafter, the resulting mixture was annealed at 923 K for 4 days. Finally, it was slowly cooled down to room temperature and a single blue crystal suitable for XRD was isolated. Qualitative energy-dispersive X-ray spectroscopy analysis detected the presence of Na, Co, Mo, and O elements (Figure 12). A polycrystalline powder of $Na_2Co_2(MoO_4)_3$ was prepared by a solid-state reaction from a stochiometric mixture of the above-mentioned reagents at 823 K.

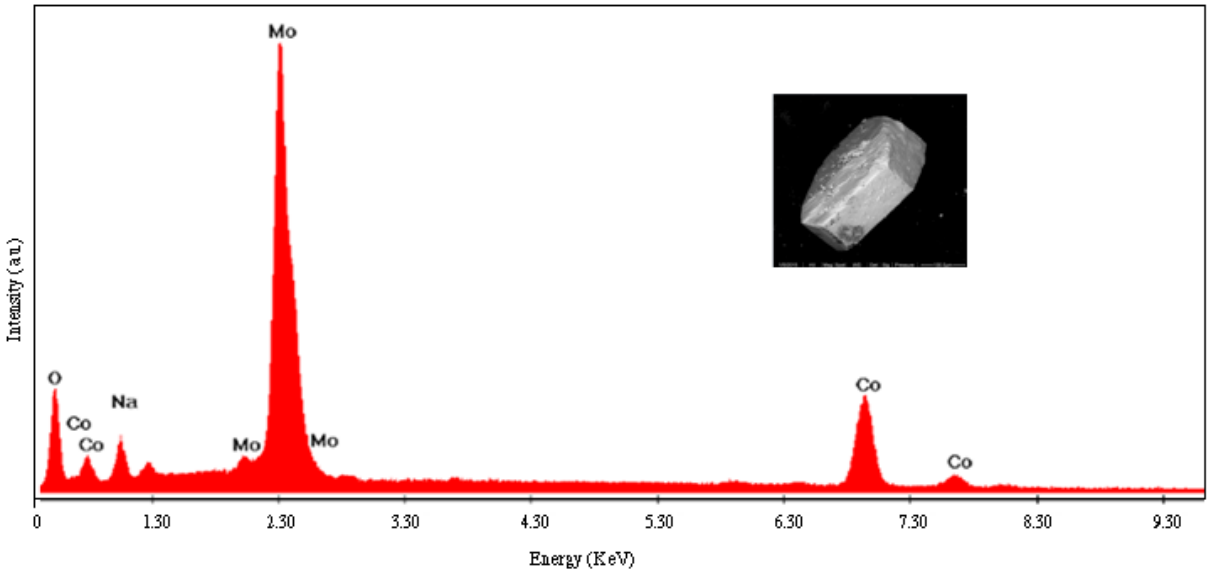

Figure 12. EDS spectrum and crystal morphology of $Na_2Co_2(MoO_4)_3$.

Acknowledgments

The authors extend their appreciation to the Deanship of Scientific Research at King Khalid University for funding this work through the research groups program under grant number R.G.P.1/25/38). The authors gratefully acknowledge Prof. Maxim Avdeev (Australian Nuclear Science and Technology Organisation) for help in bond valence calculations.

Supporting Data

A CIF file containing more details of the crystal structure was deposited in the Cambridge Crystallographic Data Centre (CCDC), 12 Union Road, Cambridge CB2 1EZ, UK; Fax: +44(0)1223-762911; email: deposit@ccdc.cam.ac.uk] (or at www.ccdc.cam.ac.uk/conts/retrieving.html) on quoting the deposit numbers CCDC429578.

References

1. Balsanova, L.; Mikhailova, D.; Senyshyn, A.; Trots, D.; Fuess, H.; Lottermoser, W.; Ehrenberg, H. *Solid State Sci.* **2009**, *11*, 1137-1143.
2. Goodenough, J. B.; Park, K. S. *J. Amer. Chem. Soc.* **2013**, *135*, 1167-1176.
3. Nagpure, I. M.; Shinde, K. N.; Kumar, V.; Ntwaeaborwa, O. M.; Dhoble, S. J.; Swart, H. C. *J. Alloys. Compd.* **2010**, *492*, 384-388.

4. Beale, A. M.; Jacques, S. D. M.; Parvalescu, E. S.; O'Brien, M. G.; Barmes, P.; Weckhuysen, B. M. *Appl. Catal.* **2009**, *A363*, 143-149.
5. Prasad, K. V. R.; Varma, K. B. R. *Ferroelectrics* **1994**, *158*, 205-210.
6. Shonai, T.; Higuchi, M.; Kodaira, K.; Ogawa, T.; Wada, S.; Machida, H. J. *Cryst. Growth* **2002**, *241*, 159-164.
7. Longoni, G.; Wang, J. E.; Jung, Y. H.; Kim, D. K.; Mari, C. M.; Ruffo, R. *J. Power Sour.* **2016**, *302*, 61-69.
8. Xiang, X.; Zhang, K.; Chen, J. *Adv. Mater.* **2015**, *27*, 5343-5364.
9. Nose, M.; Nakayama, H.; Nobuhara, K.; Yamaguchi, H.; Nakanishi, S.; Iba, H. *J. Power Sour.* **2013**, *234*, 175-179.
10. Barpanda, P.; Liu, G.; Ling, C. D.; Tamaru, M.; Avdeev, M.; Chung, S. C. Y. Yamada, A. *Chem. Mater.* **2013**, *25*, 3480-3487.
11. Deriouche, W.; Anger, E.; Freire, M.; Maignan, A.; Amdouni, N.; Pralong, V. *Solid State Sci.* **2017**, *72*, 124-129.
12. Orio, L. L.; Tillard, M.; Belin, C. *Solid State Sci.* **2008**, *10*, 5-11.
13. Okada, S.; Sawa, S.; Egashira, M.; Yamani, J.; Tabuchi, M.; Kageyama, H.; Konishi, T.; Yoshino, A. *J. Power Sour.* **2001**, *97*, 430-432.
14. Furuta, N.; Nishimura, S.; Barpanda, P.; Yamada, A. *Chem. Mater.* **2012**, *24*, 1055-1061.
15. Fu, Z.; Li, W. *Powder Diffr.* **1994**, *9*, 158-160.
16. Sarapulova, A.; Mikhailova, D.; Senyshyn, A.; Ehrenberg, H. *J. Solid State Chem.* **2009**, *182*, 3262-3268.
17. Acta CrystallogrIbers, J. A.; Smith, G. W. *Acta Crystallogr.* **1964**, *17*, 190-197.
18. Smit, J. P.; McDonald, T. M.; Poeppelmeier, K. R. *Solid State Sci.* **2008**, *10*, 396-400.
19. Xue, L.; Wang, Y.; Lv, P.; Chen, D.; Lin, Z.; Liang, J.; Huang, F.; Xie, Z. *Crystal Growth and Design* **2009**, *9*, 914-920.
20. Sebastian, L.; Piffard, Y.; Shukla, A. K.; Taulelle, F.; Gopalakrishnan, J. *J. Mater. Chem.* **2003**, *13*, 1797-1802.
21. Marzouki, R.; Guesmi, A.; Georges, S.; Zid M. F.; Driss, A. *J. Alloys. Compd.* **2014**, *586*, 74-79.
22. Ben Smida, Y.; Marzouki, R.; Georges, S.; Kutteh, R.; Avdeev, M.; Guesmi, A.; Zid, M. F. *J. Solid State Chem.* **2016**, *239*, 8-16.
23. Ben Smida, Y.; Marzouki, R.; Guesmi, A.; Georges, S.; Zid, M. F. *J. Solid State Chem.* **2015**, *221*, 132-139.
24. Georges, S.; Goutenoire, F.; Lacorre, P.; Steil, M. C. *J. Eur. Ceram. Soc.* **2005**, *25*, 3619-3627.
25. Georges, S.; Goutenoire, F.; Altorfer, F.; Sheptyakov, D.; Fauth, F.; Suard, E.; Lacorre, P. *Solid State Ionics* **2003**, *161*, 231-241.
26. Duisenberg, A. J. M. *J. Appl. Crystallogr.* **1992**, *25*, 92-96.
27. Macíček, J.; Yordanov, A. *J. Appl. Crystallogr.* **1992**, *25*, 73-80.
28. Sheldrick, G. M. *Acta Crystallogr.* **2008**, *A64*, 112-122.
29. Farrugia, L. J. *J. Appl. Crystallogr.* **1999**, *32*, 837-838.
30. North, A. C. T.; Phillips, D. C.; Mathews, F. S. *Acta Crystallogr.* **1968**, *A24*, 351-359.
31. Brown, I. D. *Phys. Chem. Miner.* **1987**, *15*, 30-34.
32. Softbv: http://kristall.uni.mki.gwdg.de/softbv.html .
33. Nespolo, M.; Ferraris, G.; Ivaldi, G.; Hoppe, R. *Acta Crystallogr.* **2001**, *B57*, 652-664.
34. Nespolo, M.; *CHARDT-IT, A Program to Compute Charge Distributions and Bond Valences in Non-molecular Crystalline Structures,* France, 2001.
35. Petricek, V.; Eigner, V.; Dusek, M.; Cejchan, A. *Z. Kristallogr.* **2016**, *231*, 301-312.
36. Petricek, V.; Dusek, M.; Plasil, *J. Z. Kristallogr.* **2016**, *231*, 583-599.

37. Nakamoto, K. *Infrared and Raman Spectra of Inorganic and Coordination Compounds*; Wiley: New York, NY, USA, 1978.

38. Marques, A. P. A.; Motta, F. V.; Cruz, M. A.; Varela, J. A.; Longo, E.; Rosa, I. L. V. *Solid State Ionics* **2011**, *202*, 54-59.

39. Hermanowicza, K.; Maczkaa, M.; Wocyrza, M.; Tomaszewskia, P. E.; Pasciaka, M.; Hanuza, J. *J. Solid State Chem.* **2006**, *179*, 685-695.

40. Selvasekarapandian, S.; Vijaykumar, M. *Mater. Chem. Phys.* **2003**, *80*, 29-33.

41. Irvine, J. T. C.; Sinclair, D. C.; West, A. R. *Adv. Mater.* **1990**, *2*, 132-138.

42. Johnson, D. *Zview version 3.1c, Scribner Associates, Inc,* **1990**.

43. Gillie, L. J.; Souza, S. A.; Sheptyakov, D.; Reeves-Mclaren, N.; Pasero, D.; West, A. R. *J. Solid State Chem.* **2010**, *183*, 2589-2597.

44. Grin, J.; Nygren, M. *Solid State Ionics* **1983**, *9*, 859-862.

45. Morales, J. P.; Herman, L.; Wang, E.; Tsai, M. T.; Lee, J. G.; Greenblatt, M. *Solid State Ionics* **1990**, *3*, 275-281.

46. Adams, S. J. *Power Sour.* **2006**, *159*, 200-204.

47. Sale, M.; Avdeev, M. *J. Appl. Crystallogr.* **2012**, *45*, 1054-1056.